

# Optimizing the interaction geometry of inverse Compton scattering x-ray sources

C.W. Sweers\* and O.J. Luiten

Department of Applied Physics, Eindhoven University of Technology,  
P.O. Box 513, 5600 MB Eindhoven, The Netherlands

(Dated: December 24, 2025)

Inverse Compton scattering is developing to be a promising method to generate coherent and tunable x-rays. In this paper we present a theoretical framework to describe an inverse Compton scattering x-ray source for arbitrary interaction angles between the electron and laser pulse. Importantly the divergence of a tightly focused laser pulse will have a significant impact of the number of scattered x-rays. The parameters of the interaction geometry are optimized for two specific cases: head-on scattering; and a grazing co-propagating interaction angle. For head-on scattering we show that a tight symmetrically focused laser pulse, that balances laser intensity and interaction time, optimizes the x-ray brilliance. For a grazing angle geometry an elliptical focus of the laser pulse is required to mitigate a reduced interaction time. We find that the latter geometry is especially useful for soft x-ray generation.

## I. INTRODUCTION

Coherent and tunable x-ray sources have become a central tool in many field of science, such as materials science [1], life sciences [2], and advanced medical diagnostics [3]. This demand is primarily served by large facilities such as synchrotrons and free electron lasers [4]. However, due to the limited availability of these large facilities, their usage comes with many logistical challenges. Therefore, there is a growing need for coherent and tunable x-ray sources at the scale of the university lab.

Inverse Compton scattering (ICS), in which relativistic electrons collide with an intense laser pulse, forms the basis of a promising method to generate x-rays at the lab scale. Several ICS based x-ray sources are currently operational [5–11] and new designs have been proposed [12–15]. Imaging techniques that require energy tunability and coherence, such as K-edge subtraction imaging [16] and phase contrast imaging [17], have been demonstrated with an ICS based x-ray source and the use of lensless techniques such as ptychography has also been proposed [18].

While the fundamental theory of ICS has been described in great detail [19–21], a closed form analytical treatment, that takes into account both the three dimensional distribution of the pulsed electron and laser beams and arbitrary interaction angles, is lacking. Optimization tasks are therefore left to simulations, which can be time consuming, and more importantly, do not provide a thorough physical understanding.

The goal of this paper is to provide an analytical closed form theoretical framework to optimize x-ray generation by ICS. The framework is meant to provide intuitive

understanding on how the x-ray source performance scales with the parameters of the interaction geometry. Here, the term *geometry* refers not only the interaction angle, but also the electron and laser pulse dimensions, the electron beam energy and the bunch charge.

The framework could serve as a baseline for a Compton x-ray source design, where given a desired x-ray energy and performance of the electron beamline and laser system, the optimized interaction geometry can be calculated directly.

## A. Basic properties of inverse Compton scattering

Figure 1a illustrates the geometry of ICS. An electron (green) with velocity  $\vec{v} = \beta c \hat{z}$  and normalized energy  $\gamma = 1/\sqrt{1 - \beta^2}$  interacts with a laser pulse (red) under an interaction angle  $\theta_L$ , w.r.t. the electron velocity. This angle is defined such that  $\theta_L = \pi$  corresponds to a head-on collision. During the interaction, the electron starts to rapidly oscillate, radiating in the process (purple). Due to the relativistic nature of the electron, the radiation becomes strongly blue shifted. The frequency up-shift is given by [21]

$$\omega_x = \omega_L \frac{1 - \beta \cos \theta_L}{1 - \beta \cos \theta_x} \quad (1)$$

Here,  $\omega_x$  and  $\omega_L$  are the angular frequencies of the radiation and the laser pulse, respectively, and  $\theta_x$  is the angle of the outgoing radiation with respect to the electron velocity.

In the relativistic limit ( $\gamma \gg 1$ ) and under small radiation angles ( $\gamma \theta_x \ll 1$ ), Eq. (1) can be approximated. For head-on scattering ( $\theta_L = \pi$ ) this results in the well known expression

$$\omega_x \underset{\theta_L=\pi}{\approx} \omega_L \frac{4\gamma^2}{1 + \gamma^2 \theta_x^2}, \quad (2)$$

\* c.w.sweers@tue.nl

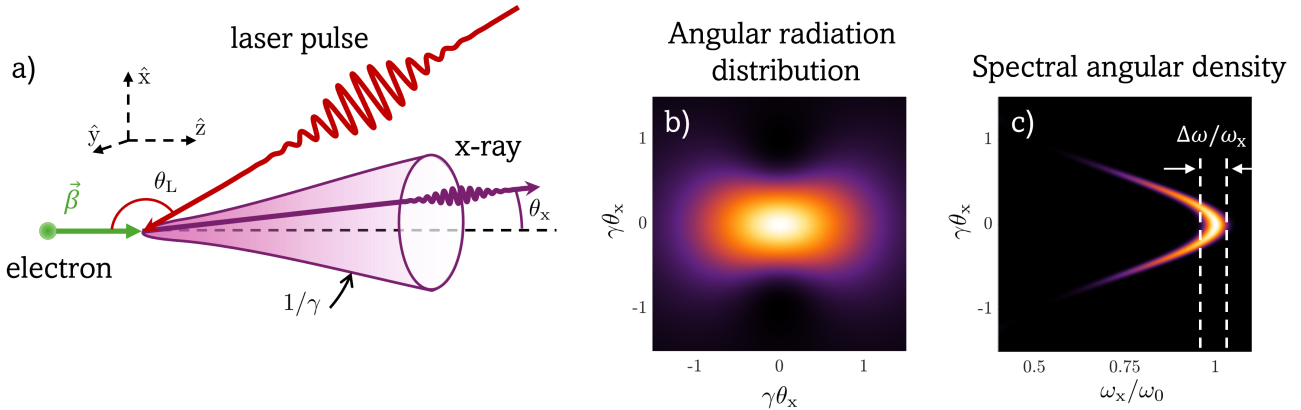


FIG. 1. a) Schematic representation of ICS. An electron (green) interacts with a laser pulse (red) under an angle  $\theta_L$ , generating an x-ray with emission angle  $\theta_x$ . b) shows the angular radiation distribution, which becomes symmetrical for  $\theta_x \ll 1/\gamma$ . Here the vertical axis is in the direction of the laser polarization. c) shows the spectral angular density, with  $\omega_0 = \omega_L(1 - \beta \cos \theta_L)/(1 - \beta)$  is the on-axis x-ray frequency.

whereas for small interaction angles ( $\theta_L \ll 1$ ) we find

$$\omega_x \underset{\theta_L \ll 1}{\simeq} \omega_L \frac{1 + \gamma^2 \theta_L^2}{1 + \gamma^2 \theta_x^2}. \quad (3)$$

Note here that, since typically a large frequency up-shift is desired,  $\gamma\theta_L \gg 1$ . These approximations clearly show that the x-ray energy can be tuned by varying either the electron energy,  $\gamma$ , or the interaction angle  $\theta_L$ .

Additionally, Eqs. (2) and (3) show how the x-ray frequency depends on the angle  $\theta_x$ , with the highest frequency emitted along the propagation direction of the electron ( $\theta_x = 0$ ) and the frequency is progressively decreasing for larger angles, as shown in Fig 1c. At  $\theta_x \simeq 1/\gamma$  the x-ray frequency has become half of the on-axis frequency. Fig 1b shows the intensity distribution of ICS, which is concentrated in a narrow cone characterized by a half angle  $\theta_x = 1/\gamma$  [22]. The distribution is slightly asymmetric for linear laser polarization, which is in Fig 1b in the vertical direction. However, for  $\theta_x \ll 1/\gamma$ , which is required for a narrow bandwidth x-ray beam, the radiation distribution is to a good approximation uniform.

The central challenge in the development of Compton x-ray sources lies in the low efficiency of x-ray generation per electron, associated with the small Thomson cross section,

$$\sigma_T = \frac{8\pi}{3} r_e^2 \simeq 66.5 \text{ fm}^2, \quad (4)$$

with  $r_e$  the classical electron radius. Obviously, for efficient generation of x-rays with a Compton source the density of electrons and laser photons needs to be as high as possible, requiring focused electron and laser pulses.

## B. Structure of this paper

We will analyze the dependence of the x-ray generation on geometry of ICS in increasing levels of complexity, illustrated by Fig. 2. We start in Sec. II by describing ICS in a head-on geometry using a collisional model. We first consider the collision between pencil beams, i.e. in the approximation of perfectly parallel beams (1 in Fig. 2). Next, we analyze the more realistic situation of a focused laser pulse and a pencil electron beam (2 in Fig. 2) and find the optimized interaction spot size and a corresponding optimized bunch charge.

In Sec. III, we analyze ICS under arbitrary interaction angles. This is the most novel part of the paper. A proper analysis of this geometry requires a treatment in a covariant framework and reveals in several subtle effects. Again, we the situation of two pencil beams (3 in Fig. 2) subsequently the situation of a focused laser pulse and a pencil electron beam (4 in Fig. 2). We derive closed form analytical expressions for the parameters that define interaction geometry which optimize the x-ray brilliance in a grazing angle geometry. We find that a shallow co-propagating interaction angle – a *grazing angle geometry* – can be favorable compared to a head-on geometry, especially for generation of soft x-rays.

## II. HEAD-ON INVERSE COMPTON SCATTERING

In this section we describe ICS in a head-on geometry ( $\theta_L = \pi$ ). We start with a pencil beam description and calculate the x-ray brilliance. The result from this simplified model serves as a demonstration of important

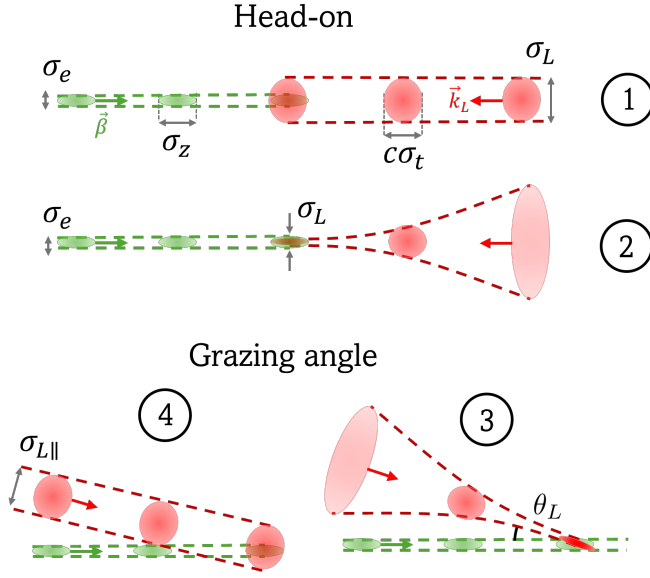


FIG. 2. Four illustrations of the geometries considered throughout this paper. In each geometry the electron bunch (green) with velocity  $\beta$  and laser pulse (red) with wave vector  $\mathbf{k}_L$  are shown at three different times up until the collision. The top figures show the pencil beam (1) and focused laser beam (2) description in a head-on geometry. The bottom figures show the pencil beam (3) and focused laser beam (4) description in a grazing angle geometry. The relevant r.m.s. pulse dimensions are also indicated

scalings for ICS. Next, we consider a finite laser pulse length to find the optimal laser waist. Finally, a simple argument is used to find the bunch charge that maximizes the x-ray brilliance.

### A. Pencil beam description

The total number of scattered photons from ICS can be calculated by considering an electron pulse and a laser pulse colliding in a head-on geometry. First we assume the pulses to be pencil beams with a Gaussian transverse photon or electron density

$$\rho_{L,e} = \frac{N_{L,e}}{2\pi\sigma_{L,e}^2} \exp\left(-\frac{x^2 + y^2}{2\sigma_{L,e}^2}\right), \quad (5)$$

where the subscripts  $L$  and  $e$  refer to either the laser or electron beam.  $N_{L,e}$  is the total number of laser photons or electrons and  $\sigma_{L,e}$  is the r.m.s. transverse size. Throughout this paper a quantity  $\sigma$  refers to an r.m.s. quantity (with the exception of the Thompson cross section  $\sigma_T$ ). Note that we can neglect the longitudinal distributions due to the head-on geometry and the pencil beam approximation. The total number of scattered x-rays in the collision is given by [23]

$$N_x = \sigma_T \int dt \int d\mathbf{x} \rho_L \rho_e |v_e - v_L| = \frac{\sigma_T N_L N_e}{2\pi(\sigma_e^2 + \sigma_L^2)}, \quad (6)$$

Note that Eq. (6) considers the x-rays scattered in the complete  $4\pi$  solid angle and the corresponding full bandwidth. If a small relative energy spread  $\Delta\omega/\omega_x$  is required, the x-ray acceptance angle should be reduced to  $\Theta_x = \sqrt{(\Delta\omega/\omega_x)}/\gamma$ . If  $\gamma\Theta_x \ll 1$ , the number of x-rays in this acceptance angle is [22]

$$N_x = \frac{\sigma_T N_L N_e}{4\pi\sigma_e^2} \frac{3}{2} \gamma^2 \Theta_x^2. \quad (7)$$

Here, we have additionally assumed the size of the electron and laser pulses to be matched ( $\sigma_L = \sigma_e$ ), which is an important assumption throughout this section. A figure of merit often used to compare x-ray sources is the x-ray brilliance, which takes into account the photon flux, transverse coherence and relative energy spread. The average r.m.s. x-ray brilliance is defined as [24]

$$B_x = \frac{f N_x}{\Delta A \Delta \Omega (\Delta\omega/\omega_x)}. \quad (8)$$

Here,  $f$  is the repetition rate,  $\Delta A$  is the x-ray source area and the  $\Delta\Omega$  is the solid angle in which the x-rays are emitted. For details regarding the definition of the x-ray brilliance, see Appendix C. Using  $\Delta A \Delta \Omega = \pi^2 \sigma_e^2 \Theta_x^2$  the average r.m.s. brilliance becomes

$$B_x = \frac{f \sigma_T N_L N_e}{4\pi^3} \frac{3}{2} \frac{1}{\Theta_x^2 \sigma_e^4} \frac{\gamma^2 \Theta_x^2}{\Delta\omega/\omega_x}. \quad (9)$$

The x-ray energy spread of a Compton x-ray source has several contributions originating from both the laser pulse and electron beam [25]. For now, to illustrate important scalings, we make a simplification and consider only the bandwidth due to the angular spread of the electron beam  $\Delta\omega/\omega_x|_{\sigma_{\theta_e}} = \gamma^2 \sigma_{\theta_e}^2$ . If we describe the electron beam using the normalized emittance,  $\epsilon_n = \gamma\beta\sigma_e\sigma_{\theta_e} \simeq \gamma\sigma_e\sigma_{\theta_e}$ , Eq. (9) can be rewritten as

$$B_x = \frac{f \sigma_T N_L N_e}{4\pi^3} \frac{3}{2} \frac{\gamma^4 \sigma_{\theta_e}^2}{\epsilon_n^4}. \quad (10)$$

Equation (10) shows two important scalings: First, we find that the brilliance scales with  $\gamma^4$ , which originates from the improved geometric emittance with increased electron energy. This not only results in a smaller x-ray source size, but also allows for tighter focusing of the laser pulse. In a head-on geometry, the electron energy is fixed by the desired x-ray energy and laser wavelength. If the interaction angle is varied, however, this scaling can be exploited for any desired x-ray energy. This will be further explored in Sec. III.

Second, Eq. (10) shows that  $B_x \propto N_e/\epsilon_n^4$ . For space charge dominated electron beams, it holds that  $N_e/\epsilon_n^2 = \text{constant}$ . As a result we find that the x-ray brilliance increases with a lower bunch charge. This counterintuitive result is a direct consequence of the assumption that the spot size of the electron and laser beams are matched ( $\sigma_L = \sigma_e$ ), which is an assumption

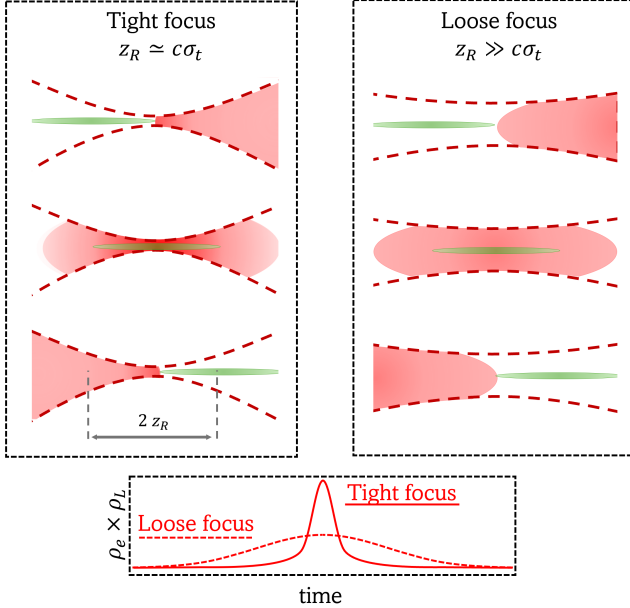


FIG. 3. Illustration of how the laser divergence effects the interaction time when the pulse length becomes comparable to the interaction length. The bottom graph shows the product of the electron and laser density as a function of time for a tight and loose focus.

that cannot hold indefinitely, as it is obviously limited by the diffraction limit. In the remainder of this section we calculate the x-ray flux and brilliance with realistic electron and laser beam descriptions, and find the optimized laser focus and the corresponding bunch charge to match the electron spot size to the laser pulse.

### B. Focused laser pulse

Before the diffraction limit is reached, the interaction time between the electron and laser pulse can become significantly reduced. This occurs when the Rayleigh range becomes similar to the laser pulse length. Not only does this impact the the total number of scattered x-rays, the energy spread is also increased. This effect is illustrated in Fig. 3. To analyze the effect of focused laser pulse we now consider the photon density of a TEM<sub>00</sub> pulsed Gaussian laser beam

$$\rho_L = \frac{N_L}{(2\pi)^{3/2} \sigma_L^2(z) \sigma_t} \exp \left[ -\frac{x^2 + y^2}{2\sigma_L^2(z)} - \frac{(z/c + t)^2}{2\sigma_t^2} \right]. \quad (11)$$

Where  $\sigma_t$  is the laser pulse length and  $\sigma_L(z) = \sigma_L(0)\sqrt{1 + (z/z_R)^2}$  with  $z_R = 2k_L\sigma_L^2$  the Rayleigh range. Throughout this paper we assume perfect laser beams ( $M^2 = 1$ ). For non-perfect laser beams the analysis still holds, however, the Rayleigh length and angular spread should be adjusted accordingly. For now, we as-

sume the electron beam to be described by a pencil beam. Integration of Eq. (6) with (11) results in

$$N_x = \frac{\sigma_T N_L N_e}{4\pi\sigma_e^2} \frac{3}{2} \gamma^2 \Theta_x^2 \sqrt{\pi} u \operatorname{erfcx}(u). \quad (12)$$

Here,  $\operatorname{erfcx}(x) = \exp(x^2)\operatorname{erfc}(x)$  is the scaled complementary error function [26], and  $u = 2z_R/c\sigma_t$ . The term  $\sqrt{\pi} u \operatorname{erfcx}(u)$  describes how the effective interaction time is reduced due to the laser divergence [19]. If we assume  $\epsilon_n/\gamma \ll \lambda_L/4\pi$ , a very reasonable assumption in practice, then also the divergence and finite longitudinal size of the electron beam,  $\sigma_z$ , can be taken into account by using  $u = 2z_R/\sqrt{(c^2\sigma_t^2 + \sigma_z^2)}$ .

To calculate the brilliance, we must now take into account the x-ray bandwidth, to which both the laser pulse and the electron beam contribute. Here we consider only the contributions of the laser pulse which has three sources. First, the Fourier limited bandwidth  $\Delta\omega/\omega_x|_{\omega_L} = 1/(2\omega_L\sigma_t)$ . However, due to the shorter interaction time, this term is broadened as

$$\Delta\omega/\omega_x|_{\omega_L} = 1/\left[2\omega_L\sigma_t\sqrt{\pi} u \operatorname{erfcx}(u)\right]. \quad (13)$$

Second, the angular spread of a focused laser pulse gives rise to a spread in the interaction angle  $\sigma_{\theta L} = 1/(2k_L\sigma_L)$ , resulting in an additional x-ray broadening. By expanding Eq. (1) around  $\theta_L = \pi$  we find  $\Delta\omega/\omega_x|_{\sigma_{\theta L}} = 1/(2k_L\sigma_L)^2$  [25], which can be expressed in terms of  $u$  as

$$\Delta\omega/\omega_x|_{\sigma_{\theta L}} = 1/(\omega_L\sigma_t u) \quad (14)$$

Finally, at high field intensities the x-ray energy spread is increased due to nonlinear broadening [27], characterized by the normalized vector potential amplitude  $A_0 = eE_0/(mc\omega_L)$ , with  $e$  the elementary charge and  $m$  the electron mass. The corresponding x-ray energy spread is [25]

$$\Delta\omega/\omega_x|_{A_0} \simeq \frac{1}{6} A_0^2 = \chi/(\omega_L\sigma_t u). \quad (15)$$

In the right equality, we have expressed the nonlinear broadening in terms of the laser pulse dimensions. Here,  $\chi = 4\sigma_T N_L/(3\sqrt{\pi}\alpha\lambda_L c\sigma_t)$  relates the laser peak power to the normalized vector potential and  $\alpha$  is the fine structure constant. The nonlinear broadening can become the significant contribution to the x-ray energy spread at tight laser focus. We note that the nonlinear broadening can be circumvented using appropriate laser pulse chirping [28].

The three energy spread contributions can be combined, resulting in the following expression for x-ray brilliance

$$B_x = \frac{3f\sigma_T N_L N_e}{4\pi\sigma_e^2} \frac{\gamma^2 \omega_L \sigma_t}{\pi^2 \sigma_e^2} \frac{\pi u^2 \operatorname{erfcx}(u)^2}{\sqrt{1 + 4\pi(1 + \chi^2)\operatorname{erfcx}(u)^2}}. \quad (16)$$

To optimize the brilliance, we note that for space charge limited electron beams  $\epsilon_n = \eta\sqrt{eN_e}$  [29], where  $\eta$  is a property of the injector that describes the electron beam emittance at given bunch charge. Therefore  $N_e/\sigma_e^2 = \text{constant}$ . Since  $u \propto \sigma_L^2 = \sigma_e^2$ , the function  $g(u) = \pi u \operatorname{erfcx}(u)^2 / \sqrt{1 + 4\pi(1 + \chi^2)\operatorname{erfcx}(u)^2}$  needs to be maximized, resulting in the optimized value for  $\sigma_e$  that maximizes the x-ray brilliance

$$\sigma_e^{\text{opt}} = \sqrt{u_{\text{max}} \lambda_L c \sigma_t / 8\pi} \quad (17)$$

where  $u_{\text{max}}$  is the value of  $u$  that maximizes  $g(u)$ . To take into account the electron pulse length  $\sigma_z$ , the substitution  $\sigma_t \rightarrow \sigma_t \sqrt{1 + (\sigma_z/c\sigma_t)^2}$  should be used in Eq. (17). To take into account the bandwidth contributions from the electron beam, additional terms should be added to the square root of  $g(u)$  which lowers the value in  $u_{\text{max}}$ .

The green and blue curves in Fig. 4 show the functions  $g(u)$  for  $\chi = 0$  and  $\chi = 5$ , respectively. The inset show  $u_{\text{max}}$  as a function of  $\chi$ . The yellow curve shows the function  $1/u$ , which corresponds to the brilliance scaling of the pencil beam limit.

This analysis has been done under the assumption that the electron and laser spot sizes are matched,  $\sigma_e = \sigma_L$ . At a fixed energy, the electron spot size is determined by the beam divergence  $\sigma_{\theta e}$  and normalized emittance  $\epsilon_n$ . Due to practical considerations, for relativistic beams,  $\sigma_{\theta e}$  is typically limited a few milliradians. We therefore consider a fixed electron divergence and optimize the normalized emittance such that  $\sigma_e = \sigma_L$ . To arrive at an expression for the optimized bunch charge we use the fact that  $\epsilon_n = \eta\sqrt{eN_e} = \gamma\sigma_e\sigma_{\theta e}$ , combined with Eq. (17). This results in

$$eN_e^{\text{opt}} = u_{\text{max}} \gamma^2 \sigma_{\theta e}^2 \frac{\lambda_L c \sigma_t}{8\pi\eta^2}, \quad (18)$$

which is the bunch charge that allows for the optimized electron spot size  $\sigma_e^{\text{opt}}$ .

### C. Optimized head-on geometry

As an example, we calculate the brilliance of an ICS source generating 10 keV x-rays in a head-on geometry. The electron bunches are generated from a C-band photoinjector [30] that is able to create 200 pC electron bunches at  $\epsilon_n = 200$  nmrad ( $\eta = 14$  nmrad/ $\sqrt{\text{pC}}$ ) and a relative energy spread of 0.2%. The electrons are accelerated to  $\gamma = 46$  to generate 10 keV x-rays with a 5 mJ, 100 fs, 1030 nm interaction laser pulse [31]. We assume the electron pulse length to be matched to the laser pulse length. Both the photoinjector and laser system operate at  $f = 1$  kHz.

Figure 5 shows the x-ray brilliance at a varying bunch charge where it is assumed that  $\sigma_L = \sigma_e = \epsilon_n / (\gamma\sigma_\theta)$ .

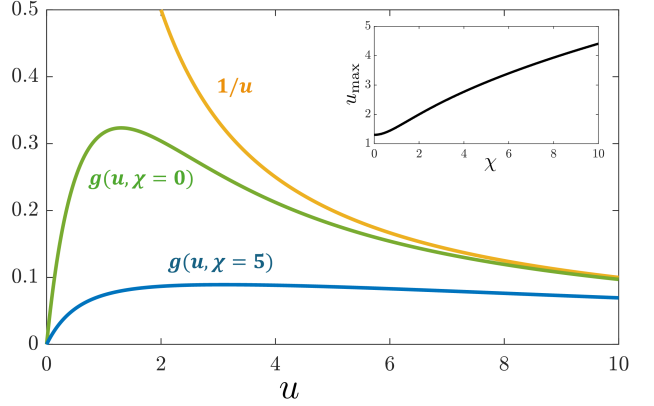


FIG. 4. Plots of the function  $g(u)$  for  $\chi = 0$  (green) and  $\chi = 5$  (blue). The inset shows value of  $u_{\text{max}}$  for varying values of  $\chi$ . The green curve shows the function  $1/u$  corresponding to the brilliance scaling of the pencil beam limit.

Here we have also included the energy spread contributions from the electron beam. The continuous curve is calculated using Eq. (16), and the dots are the result of particle tracking simulations (General Particle Tracer [32]) and subsequent numerical calculation of the Liénard-Wiechert potentials [33]. At these parameters  $\chi = 5.6$  and  $\sigma_e^{\text{opt}} = 2.4 \mu\text{m}$ . With an electron divergence angle of  $\sigma_\theta = 1$  mrad, the optimized bunch charge is 43 pC.

At the relatively low bunch charge of 43 pC, the x-ray brilliance is 10 times higher than at 1 nC. Additionally, the total number of scattered x-rays is only 4% lower at 43 pC than at 1 nC. Due to the optimization of the laser focus and bunch charge, ICS becomes significantly more efficient at 20 times lower bunch charge. This can be a very important design consideration regarding background suppression and radiation protection.

## III. INVERSE COMPTON SCATTERING FOR ARBITRARY INTERACTION ANGLES

In this section we investigate how to make use of the fact that a Compton x-ray source becomes more efficient at high electron energies. In a head-on geometry, the desired x-ray energy determines electron energy. However, if instead the interaction angle is varied to achieve the required x-ray energy, the favorable scaling with electron beam energy can be exploited even further. We will find that this geometry can be particularly useful for soft x-ray generation

We will now use the framework of covariant electrodynamics, with the metric,  $g^{\mu\nu} = \text{diag}(1, -1, -1, -1)$ , to describe the interaction of a relativistic electron bunch with a laser pulse under an arbitrary interaction angle.

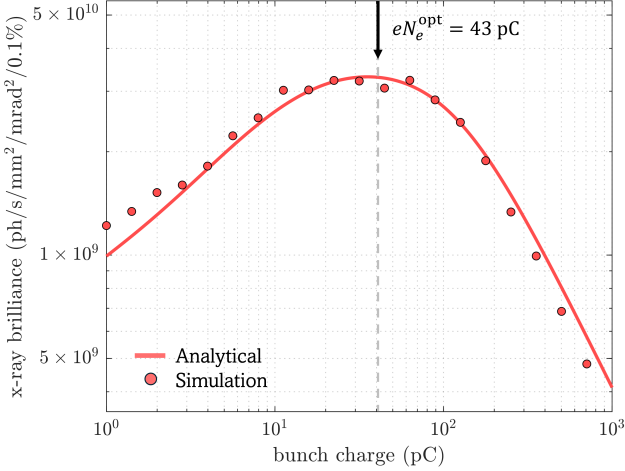


FIG. 5. X-ray brilliance in for 10 keV x-ray generation in a head-on geometry for varying bunch charge and matched electron and laser spot sizes. The analytical result of Eq. (16) (solid curve) agrees well with simulation results (dots). The arrow marks the theoretical optimized bunch charge according to Eq. (18)

We start by considering a single electron interacting with a Gaussian pencil beam. Next, we add the effects of a focused laser beam and describe the electron bunch as a finite sized object. In Sec.III D the case where  $\theta_L \ll 1$  is considered and the x-ray brilliance is optimized for this grazing angle geometry. Finally, a comparison is made between grazing angle and head-on ICS.

### A. Single electron with a pencil laser beam

In the regime where electron recoil can be ignored, *i.e.*  $\hbar\omega_x/\gamma m_e c^2 \ll 1$ , a single electron with 4-trajectory  $x^\mu(\tau)$  and 4-velocity  $u^\mu(\tau)$  radiates, according to the Liénard-Wiechert potentials, with a spectral angular density [19]

$$\mathcal{S}(\omega, \theta_x) = \frac{\partial^2 N_x}{\partial \omega \partial \Omega} = \frac{\alpha \omega_x}{4\pi^2} \left| \int u^\mu \exp(i k_x^\nu x_\nu) d\tau \right|^2 \quad (19)$$

Here  $k_x^\mu = k_x(1, \mathbf{n}_x)$  is the four-wave vector of the scattered x-ray with  $\mathbf{n}_x$  its propagation direction.  $x^\mu = (ct, \mathbf{x})$  is the electron four-position,  $u^\mu = \gamma(1, \beta)$  its normalized four-velocity, and  $\tau = t/\gamma$  is the proper time.

The x-ray brilliance is closely related to the spectral angular density. In the approximation  $\sigma_e \ll \sigma_L$ ,

$$B_x \simeq \frac{f N_e}{\pi \sigma_e^2} \omega_x \mathcal{S}(\omega_x, 0). \quad (20)$$

The dimensionless quantity  $\omega_x \mathcal{S}(\omega_x, 0)$  is the peak normalized spectral angular density, which is maximized

at  $\theta_x = 0$  and when  $\omega = \omega_x$ . In this section we will analyze how  $\omega_x \mathcal{S}(\omega_x, 0)$  depends on the interaction geometry of ICS. Specifically, how it depends on the laser pulse dimensions, interaction angle and electron energy.

The integral in Eq. (19) is solved by considering a single electron that experiences the normalized vector potential, with amplitude  $A(\tau)$ , of the laser pulse. We assume that this normalized vector potential is Gaussian, *i.e.*  $A(\tau) = A_0 \exp(-\tau^2/2\tau_{\text{int}}^2)$ . Here,  $\tau_{\text{int}}$  is the proper interaction time of the electron with the laser pulse. Note that  $\tau_{\text{int}}$  does *not* equal the laser pulse length. How  $\tau_{\text{int}}$  relates to the laser pulse parameters is discussed later.  $A_0$  can be written in terms of the laser pulse dimensions

$$A_0^2 = \frac{3\sigma_T N_L}{2\alpha\pi^{3/2}} \frac{1}{\sigma_{L\parallel}\sigma_{L\perp}\omega_L\sigma_t}. \quad (21)$$

Due to the asymmetry in the interaction geometry, we also consider an asymmetric laser pulse focus with two transverse sizes,  $\sigma_{L\parallel}$  and  $\sigma_{L\perp}$ . Here, the subscripts  $\parallel$  and  $\perp$  refer to the directions parallel and perpendicular to the x-z plane, respectively.

When nonlinear effects can be neglected, *i.e.*  $A_0 \ll 1$ , the peak normalized spectral angular density from a single electron is given by the concise expression

$$\omega_x \mathcal{S}(\omega_x, 0) = \frac{1}{8\pi} \alpha A_0^2 \omega_x^2 \tau_{\text{int}}^2 \quad (22)$$

For details, we refer to Appendix A. In this expression all dependencies on the interaction geometry are implicit in  $A_0$  and  $\tau_{\text{int}}$ . In a head-on geometry ( $\theta_L = \pi$ ) the proper interaction time  $\tau_{\text{int}} = c\sigma_t/[\gamma(1 + \beta)]$ , while for  $\theta_L = 0$ , it becomes  $\tau_{\text{int}} = c\sigma_t/[\gamma(1 - \beta)]$ .

For intermediate interaction angles,  $0 < \theta_L < \pi$ ,  $\tau_{\text{int}}$  depends on  $\sigma_{L\parallel}$ . This effect is explained in Fig. 6a, in which the electron (green) crosses the laser pulse (red) under an angle  $\theta_L$ . The vector potential amplitude, as experienced by the electron, is illustrated by the red solid curve. Due to the finite value of  $\sigma_{L\parallel}$ , the time that electron and laser pulse overlap is reduced. In the co-moving frame (Fig. 6b) this can be understood as the electron experiencing a tilted laser pulse front. Therefore, the experienced vector potential amplitude becomes a function of both the pulse length,  $\sigma_t$  and transverse size  $\sigma_{L\parallel}$ .

The reduction in the interaction time can be quantified by a dimensionless parameter  $\zeta \in [0, 1]$ , defined as the ratio between the proper interaction time and the Lorentz transformed laser pulse length, and is given by

$$\zeta = \left[ 1 + \left( \frac{\beta \sin \theta_L}{1 - \beta \cos \theta_L} \frac{c\sigma_t}{\sigma_{L\parallel}} \right)^2 \right]^{-1/2}. \quad (23)$$

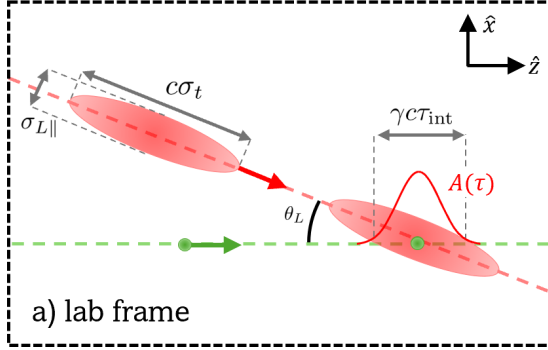


FIG. 6. Illustrations on how the proper interaction time  $\tau_{\text{int}}$  is reduced by  $\sigma_{L\parallel}$  in both the lab frame (a) and the co-moving frame (b).

Consequently, the proper interaction time is given by

$$\tau_{\text{int}} = \frac{\sqrt{2}\sigma_t\zeta}{\gamma(1 - \beta \cos \theta_L)} \simeq 2\sqrt{2}\gamma\sigma_t\zeta\omega_L/\omega_x, \quad (24)$$

where we used  $\gamma \gg 1$  in the approximation on the right.

Figure 7 shows how  $\zeta$  changes with the interaction angle for various aspect ratios,  $\sigma_{L\parallel}/c\sigma_t$ . In a head-on geometry ( $\theta_L = \pi$ ), it is obvious that  $\zeta = 1$ . For  $\theta_L = 0$  the laser pulse is propagating in the same direction as the electron beam and again  $\zeta = 1$ . However, for  $0 < \theta_L < \pi$ , the interaction time strongly depends on  $\theta_L$ . The effect of  $\zeta$  is most extreme at small interaction angles, a *grazing angle geometry*, with a minimum at  $\theta_L = \cos^{-1}(\beta) \simeq 1/\gamma$ .

The effect of the reduced overlap can be overcome by either applying a pulse front tilt to the laser that corrects for the tilted front in the co-moving frame [34–36]; or by utilizing a line focused laser pulse, where  $\sigma_{L\parallel} \gg \sigma_{L\perp}$ . In this work we will analyze the second solution.

As an example, a 100 fs laser pulse focused to  $\sigma_L = 2.4 \mu\text{m}$  interacting under  $\theta_L = 10^\circ$  at  $\gamma = 50$ , gives rise to a reduction of the interaction time with  $\zeta = 0.007$ . As a result the brilliance is reduced by more

than 4 orders of magnitude. Utilizing a line focus, with aspect ratio  $\sigma_{L\parallel}/\sigma_{L\perp} = 100$ , we find that  $\zeta = 0.58$ . While the laser intensity is now lower (by a factor of 100), the x-ray brilliance is almost two orders of magnitude higher than if a tight symmetrical focus was applied.

The blue curve in Fig. 7 shows that also for small deviations from  $\theta_L = \pi$  the interaction time can become significantly reduced when utilizing a tight laser focus. This suggest that in a head-on geometry, it may pay off to approach  $\theta_L = \pi$  as closely as possible, for instance by using parabolic mirrors with through holes [37].

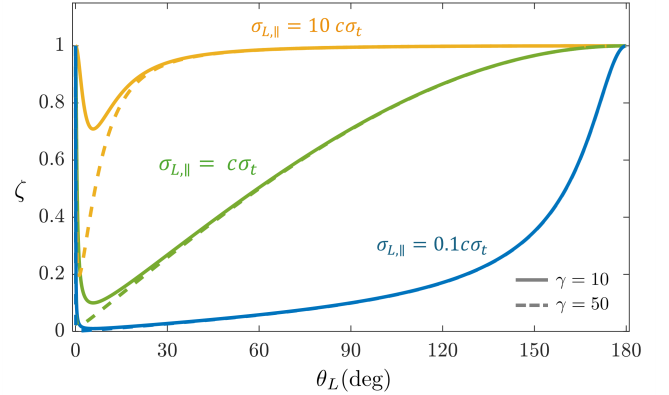


FIG. 7.  $\zeta$  as a function of the interaction angle for three different ratios of  $\sigma_{L\parallel}/c\sigma_t$ . The solid curves correspond to  $\gamma = 10$ , whereas the dashed curves correspond to  $\gamma = 50$ .

In Sec. III D we will find expressions for the optimized laser pulse dimensions. To find these, however, we first need to describe the effect of focused laser pulse for arbitrary interaction angles.

## B. Single electron with a focused laser beam

Similar to Sec. II B we have found that a tight laser focus is required to optimize the ICS interaction. Therefore we need to consider the effect of a focused laser pulse. In contrast to Sec. II B, we now only have a tight focus in the  $y$ -direction. Additionally, since the interaction angle is no longer parallel to the electron velocity, the electron no longer traverses the complete longitudinal profile of the laser pulse. The effect of a focused laser pulse for grazing angle ICS is analyzed using the substitution  $A(\tau) \rightarrow A(\tau)/\sqrt{1 + \tau^2/\tau_R^2}$ , similar to the method presented in [38]. Here we have introduced a proper Rayleigh time,

$$\tau_R = \frac{4k_L\sigma_{L\perp}^2}{\gamma\beta c \cos \theta_L} \left(1 + \frac{\sigma_{L\perp}^4}{\sigma_{L\parallel}^4}\right)^{-1/2}, \quad (25)$$

which describes the proper time that the electron spends within the Rayleigh range of the laser pulse. When this time becomes small compared to the interaction time the number of scattered photons is reduced and the x-ray bandwidth is increased. The effect can be taken into account by the substitution

$$\tau_{\text{int}} \rightarrow \tau_{\text{int}} \psi \mathcal{K}_0(\psi^2/4) \quad (26)$$

with  $\mathcal{K}_0(x) = \exp(x)K_0(x)/\sqrt{2\pi}$  the exponentially scaled Bessel function of second kind and order zero, and  $\psi = \tau_R/\tau_{\text{int}}$ . The role of  $\psi$  is also similar to that of  $u$  from Sec. II B. However,  $\psi$  describes the effect of laser pulse divergence on the interaction time at any interaction angle. In a head-on geometry,  $\psi = u$ . This result is very similar of the result from Eq. (12) since  $\sqrt{\pi} \operatorname{erfc}x \simeq \mathcal{K}_0(x^2/4)$ .

In a line focus geometry, where  $\sigma_{L\perp} \ll \sigma_{L\parallel}$ ,  $\psi$  can be rewritten as

$$\psi \simeq \frac{1 - \beta \cos \theta_L}{\beta \cos \theta_L} \frac{2k_L^2 \sigma_{L\perp}^2}{\omega_L \sigma_t \zeta} \quad (27)$$

When the interaction angle  $\theta_L \ll 1$ ,  $\psi \propto 1/\gamma^2$ . This is a consequence of the long interaction length,  $\gamma\beta c\tau_{\text{int}}$ , in a grazing angle geometry with a line focused laser pulse. Therefore,  $\sigma_{L\perp}$  needs to be larger, compared to the head-on case, to ensure that the Rayleigh length in the perpendicular direction does not reduce the interaction time. In Sec. III D we will find an expression for  $\sigma_{L\perp}$  that optimizes the x-ray brilliance.

In addition to a reduced interaction time, the angular spread of the focused laser pulse also induces an additional x-ray bandwidth that is not yet included in Eq. (26). The angular spread introduces a spread in the Doppler shift. This can be quantified by an expansion of Eq. (1) around  $\theta_L$ , resulting in

$$\Delta\omega/\omega_x|_{\sigma_{\theta_L}} = \frac{\beta \cos \theta_L}{1 - \beta \cos \theta_L} (\sigma_{\theta L\parallel}^2 + \sigma_{\theta L\perp}^2). \quad (28)$$

Here  $\sigma_{\theta L\parallel}$  and  $\sigma_{\theta L\perp}$  are angular spreads of the laser pulse parallel and perpendicular to the x-z plane respectively. We note that one would also expect a term in Eq. (28) that is first order in  $\sigma_{\theta L\parallel}$ , however this term is already taken into account by  $\zeta$ . For a line focused laser pulse, Eq. (28) can be rewritten as

$$\Delta\omega/\omega_x|_{\sigma_{\theta_L}} = 1/(\omega_L \sigma_t \zeta \psi). \quad (29)$$

Eq. (22) only takes into account the Fourier limited bandwidth

$$\Delta\omega/\omega_x|_{\omega_L} = 1/[2\omega_L \sigma_t \zeta \psi \mathcal{K}_0(\psi^2/4)]. \quad (30)$$

By combining the above two expressions, we find the following expression for the peak normalized spectral angular density

$$\omega_x \mathcal{S}(\omega_x, 0) = \frac{1}{\pi} \alpha A_0^2 \gamma^2 \omega_L^2 \sigma_t^2 \zeta^2 \frac{\psi^2 \mathcal{K}_0(\psi^2/4)^2}{\sqrt{1 + 4\mathcal{K}_0(\psi^2/4)^2}} \quad (31)$$

Other bandwidth contributions can be included in the same method as discussed Sec. II B. For the laser parameters under consideration, the bandwidth due to nonlinear broadening can be neglected due to the use of the line focus.

### C. Focused electron and laser beams

Up to now, we have only considered the interaction of a single electron with the laser pulse. We will now also take into account the finite electron bunch size and angular spread by means of correction terms.

The finite size of the electron beam can be taken into account by considering an electron with offset  $(x, y, z)$  at  $t = 0$ . This electron will probe a lower intensity of the laser pulse and therefore radiate fewer x-rays. Note that the x-ray bandwidth remains unaffected. For an electron bunch with initial density distribution

$$\rho_e(t = 0) = \frac{N_e}{(2\pi)^{3/2} \sigma_e^2 \sigma_z} \exp\left(-\frac{x^2 + y^2}{2\sigma_e^2} - \frac{z^2}{2\sigma_z^2}\right), \quad (32)$$

we find that the total number of scattered x-rays is reduced by a factor  $1 + \Sigma$ , where

$$\Sigma = \frac{\sigma_e^2 (1 - \beta \cos \theta_L - \sin^2 \theta_L)^2 / \beta^2 + \sigma_z^2 \sin^2 \theta_L}{4\sigma_{L\parallel}^2 (1 - \beta \cos \theta_L)^2 + 4\beta^2 c^2 \sigma_t^2 \sin^2 \theta_L} + \frac{\sigma_e^2}{4\sigma_{L\perp}^2}. \quad (33)$$

In a head-on geometry, this expression reduces to

$$\Sigma_{\theta_L=\pi} = \frac{\sigma_e^2}{4\sigma_{L\parallel}^2} + \frac{\sigma_e^2}{4\sigma_{L\perp}^2}. \quad (34)$$

By expanding Eq. (33) around  $\theta_L = 0$  and assuming that  $\sigma_{L\perp} \ll \sigma_{L\parallel}$ , we find that

$$\Sigma_{\theta_L \ll 1} \simeq \frac{\sigma_e^2}{4\sigma_{L\perp}^2} + \frac{\sigma_z^2}{\sigma_{L\parallel}^2} \gamma^4 \theta_L^2 \quad (35)$$

The important result here is that the electron pulse length,  $\sigma_z$ , starts to have a significant influence on the total x-ray flux compared to the head-on case. Note that  $\gamma\theta_L \gg 1$ , even in a grazing angle geometry (See Eq. (3)).

Besides the well known bandwidth contribution of the electron angular spread due to the spread in emission angle,  $\Delta\omega/\omega_x|_{\sigma_{\theta_x}} = \gamma^2 \sigma_{\theta_e}^2$ , in a grazing angle geometry we

also have to take into account that the electron angular spread changes the interaction angle. This creates an x-ray bandwidth contribution

$$\Delta\omega/\omega|_{\sigma_{\theta e}} = \frac{\beta \sin \theta_L}{1 - \beta \cos \theta_L} \sigma_{\theta e} \simeq \sqrt{\frac{\omega_x}{\omega_L}} 2\gamma \sigma_{\theta e}. \quad (36)$$

The approximation on the right hold for  $\theta_L \ll 1$ .

The last effect we have to take into account is interaction length,  $\gamma\beta c\tau_{\text{int}}$ , becoming longer than to the electron beta function,  $\beta = \epsilon_n/(\gamma\sigma_{\theta e}^2)$ . In this regime the x-ray source size varies during the interaction and we can no longer use the electron beam size in the focus as the x-ray source size. Instead we have to use the effective x-ray source size, obtained by a laser intensity- weighted average of the electron beam size:

$$\sigma_{e,\text{eff}}^2 = \sigma_e^2 \left[ 1 + \frac{1}{2} \left( \gamma^2 \sigma_{\theta e}^2 c\tau_{\text{int}} / \epsilon_n \right)^2 \right]. \quad (37)$$

Equation (37) should be substituted in Eq. (20). It is not required to apply the substitution in Eq. (33) since we will find that in the above mentioned regime, the electron beam becomes very small compared to the laser focus.

#### D. Optimization of a grazing angle interaction geometry

We now have all ingredients in place to optimize the interaction geometry of grazing angle ICS. To arrive at closed form analytic expressions, we first consider the interaction of a single electron with a focused laser pulse and optimize the peak normalized spectral angular density. Next we add the contributions for a realistic electron beam to calculate the corresponding x-ray brilliance. As a final step, we investigate the behavior for small interaction angles  $\theta_L \ll 1$ , to find the optimized electron energy. This method yields analytical expressions for the laser pulse dimensions, interaction angles and electron energy, for a desired x-ray energy.

For the interaction of a single electron, we optimize the peak normalized spectral angular density given by Eq. (31), to find optimized values of  $\sigma_{L\parallel}$  and  $\sigma_{L\perp}$ . The dependency on the laser pulse dimensions is implicit in  $A_0$  and  $\zeta$ , given by Eqs. (21) and (23) respectively. We now consider a line focused geometry such that  $\psi$  is given by Eq. (27), and recognize that  $A_0^2 \propto 1/\sigma_{L\parallel}\sigma_{L\perp}$ . We now find that function that the peak normalized spectral angular density is scales as

$$\omega_x \mathcal{S}(\omega_x, 0) \propto \psi^{3/2} h(\psi) \zeta^{3/2} / \sigma_{L\parallel} \quad (38)$$

$$\text{with } h(\psi) = \frac{\mathcal{K}_0(\psi^2/4)^2}{\sqrt{1 + \mathcal{K}_0(\psi^2/4)^2}}.$$

The optimized  $\sigma_{L\parallel}$  is found by maximizing  $\zeta^{3/2}/\sigma_{L\parallel}$ ,

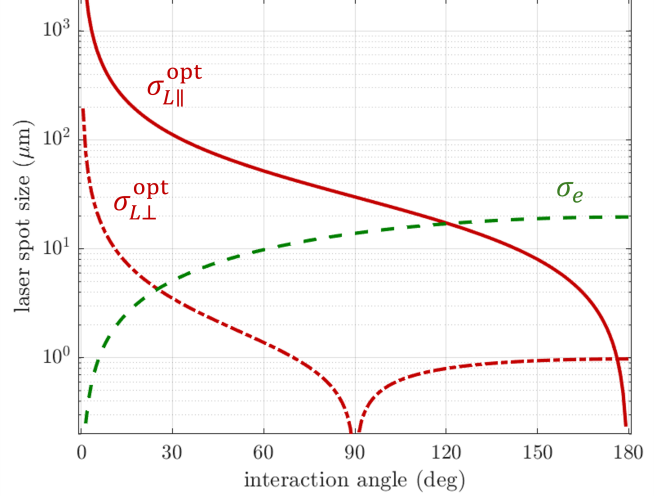


FIG. 8. Optimized laser spot sizes (red),  $\sigma_{L\parallel}^{\text{opt}}$  and  $\sigma_{L\perp}^{\text{opt}}$ , for the generation of 500 eV x-rays at varying interaction angles. The green curve shows the electron spot size at this interaction angle.

which occurs when

$$\sigma_{L\parallel}^{\text{opt}} = \frac{1}{\sqrt{2}} \frac{\sin \theta_L}{1 - \beta \cos \theta_L} \beta c \sigma_t. \quad (39)$$

Under this condition,  $\zeta = \sqrt{1/3}$ . Next, to find the optimized  $\sigma_{L\perp}$ , we optimize  $\psi^{3/2} h(\psi)$ , which has a maximum at  $\psi_{\text{max}} = 1.91$ . When taking into account additional bandwidth contributions such as the electron energy spread, resulting additional terms in the denominator of  $h(\psi)$ . This will have the effect of decreasing  $\psi_{\text{max}}$ .

Substitution of  $\zeta = \sqrt{1/3}$  and  $\psi = \psi_{\text{max}}$  into Eq. (27), we also find an expression for the optimized  $\sigma_{L\perp}$ :

$$\sigma_{L\perp}^{\text{opt}} = \frac{1}{2} \sqrt{\frac{c\sigma_t}{k_L} \left| \frac{\beta \cos \theta_L}{1 - \beta \cos \theta_L} \right| \sqrt{\frac{1}{3} \psi_{\text{max}}}}. \quad (40)$$

The absolute value signs are required since the argument becomes negative when  $\theta_L > 90^\circ$ .

The red curves in Fig. 8 show the optimized laser spot sizes  $\sigma_{L\parallel}$  and  $\sigma_{L\perp}$  for the generation of 500 eV x-rays under different interaction angles, according to Eqs. (39) and (40). The figure shows that for small interaction angles the optimal laser spot sizes become large in both directions, however the line focus is still maintained. The dashed green curve shows  $\sigma_e$  for  $\epsilon_n = 200$  nmrad and  $\sigma_\theta = 1$  mrad. Since the optimized laser spot sizes can become very small outside of the grazing angle geometry,  $\sigma_e$  should always be used as a lower bound to  $\sigma_L$ .

The x-ray brilliance can be calculated by including the effects of the finite electron beam and effective spot size

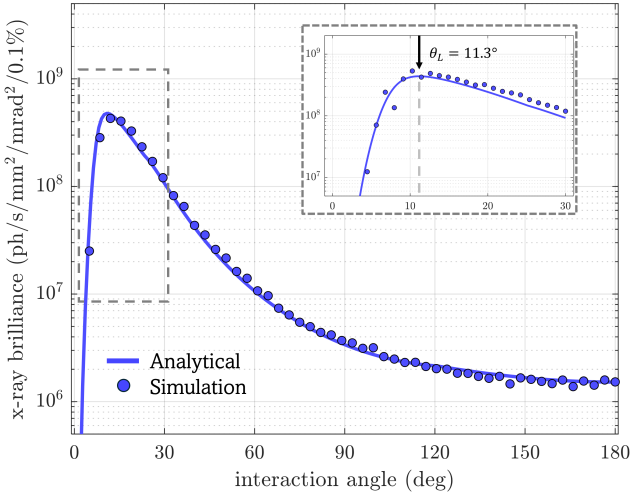


FIG. 9. X-ray brilliance for the generation of 500 eV x-rays as the interaction angle is varied and the laser spot sizes are  $\sigma_{L\parallel}^{\text{opt}}$  and  $\sigma_{L\perp}^{\text{opt}}$ . The inset shows a zoom in between 0-30 degrees, where the arrow denotes interaction angle corresponding to the optimized electron energy  $\gamma_{\text{opt}}$

into Eq. (20), resulting in

$$B_x = \frac{f N_e}{\pi \sigma_e^2 (1 + \kappa^2/2)} \frac{1}{1 + \Sigma} \omega_x \mathcal{S}(\omega_x, 0). \quad (41)$$

Here, we have introduced  $\kappa = \gamma^2 \sigma_{\theta e}^2 c \tau_{\text{int}} / \epsilon_n$  which corrects for the effective spot size over the interaction length. For arbitrary interaction angles and beam dimensions the parameters  $\zeta, \psi$  and  $\Sigma$  should be calculated using Eqs. (23), (25) and (33), respectively. However, in the optimized grazing angle geometry,  $\zeta = \sqrt{1/3}$ ,  $\psi = 1.91$ , and  $\Sigma$  is becomes

$$\Sigma = \frac{\sigma_z^2}{6 \beta^2 c^2 \sigma_t^2}. \quad (42)$$

Figure 9 shows x-ray brilliance for the generation of 500 eV x-rays as the interaction angle is varied and the laser pulse dimensions are changed along according to Eqs. (39) and (40). The electron beam  $\epsilon_n = 200$  nmrad and  $\sigma_{\theta e} = 1$  mrad. The electron energy is determined by the interaction angle and the fixed x-ray energy of 500 eV. Here  $\sigma_e$  is used as a lower bound for  $\sigma_{L\parallel}$  and  $\sigma_{L\perp}$ .

The figure clearly shows how the brilliance increases for smaller interaction angles. However, because the effective source size becomes large at very small interaction angles, the brilliance drops significantly in this range. This results in an optimal interaction angle of equivalent interaction angle. To find an expression this optimized electron energy, we analyze how  $\sigma_{L\parallel}^{\text{opt}}$  and  $\sigma_{L\perp}^{\text{opt}}$  scale for large electron energy. By series expansion of Eq. (1) for

$\theta_L \ll 1$  we find that

$$\sigma_{L\parallel}^{\text{opt}} \simeq \sqrt{\frac{\omega_L}{\omega_x}} 2\gamma c \sigma_t, \quad (43)$$

$$\sigma_{L\perp}^{\text{opt}} \simeq \sqrt{\frac{\psi_{\text{max}}}{\omega_x \sigma_t}} \sqrt{\frac{1}{3}} \gamma c \sigma_t. \quad (44)$$

Here we also find the aspect ratio of the line focus to be  $\sigma_{L\parallel}/\sigma_{L\perp} \simeq 2.15 \sqrt{\omega_L \sigma_t / \psi_{\text{max}}}$ . Since the laser spot sizes in both directions become linear with the electron energy, the peak normalized spectral angular density becomes constant w.r.t.  $\gamma$ . As a consequence the x-ray brilliance scales according to

$$B_x \propto \frac{1}{\sigma_{e,\text{eff}}^2} = \frac{\sigma_{\theta e}^2}{\epsilon_n^2} \frac{\gamma^2}{1 + \kappa^2/2}. \quad (45)$$

Since  $\kappa \propto \gamma^3$ , we can find the electron energy,  $\gamma_{\text{opt}}$ , that optimizes the x-ray brilliance:

$$\gamma_{\text{opt}} = \left[ \frac{\omega_L \sigma_{\theta e}^2}{\omega_x \epsilon_n} 4c \sigma_t \zeta \psi \mathcal{K}_0(\psi^2/4) \right]^{-1/3}. \quad (46)$$

Using Eq. (46) with (1) the corresponding interaction angle is found. As an example for the parameters used in Fig. 9, the optimized electron energy  $\gamma = 103$  and the corresponding optimized interaction angle  $\theta_L = 11.3^\circ$ . This agrees well to the result shown in Fig. 9.

Finally Eqs. (39) and (40) are used to find the optimized laser pulse dimensions, resulting the optimized grazing angle interaction geometry.

### E. Performance of a grazing angle soft x-ray Compton source

As an example, we apply the developed framework for the design of a soft x-ray Compton source with continuous tunability between 0.25 keV and 2.0 keV. This energy range has strong interest in life sciences [39, 40] and catalysis [41, 42]. In this energy range achromatic reflective x-ray optics with focal lengths below 1 meter are available [43], which could keep the footprint within the scale of a university lab.

The electron beamline is based on a high repetition rate C-band photoinjector [30]. This injector creates  $Q = 200$  pC electron bunches with normalized emittance of  $\epsilon_n = 200$  nmrad ( $\eta = 14$  nmrad/ $\sqrt{\text{pC}}$ ) and 0.2% energy spread at a repetition rate of  $f = 1$  kHz. Subsequent LINACs can be used to accelerate the electrons to the required energy. The electrons are focussed to the interaction point with an angular spread of  $\sigma_{\theta e} = 1$  mrad. The interaction laser is a 100 fs, 5mJ, Yb-fiber system with a central wavelength at 1030 nm, also operating at 1 kHz [31]. We assume the electron pulse length to be matched to the laser pulse length.

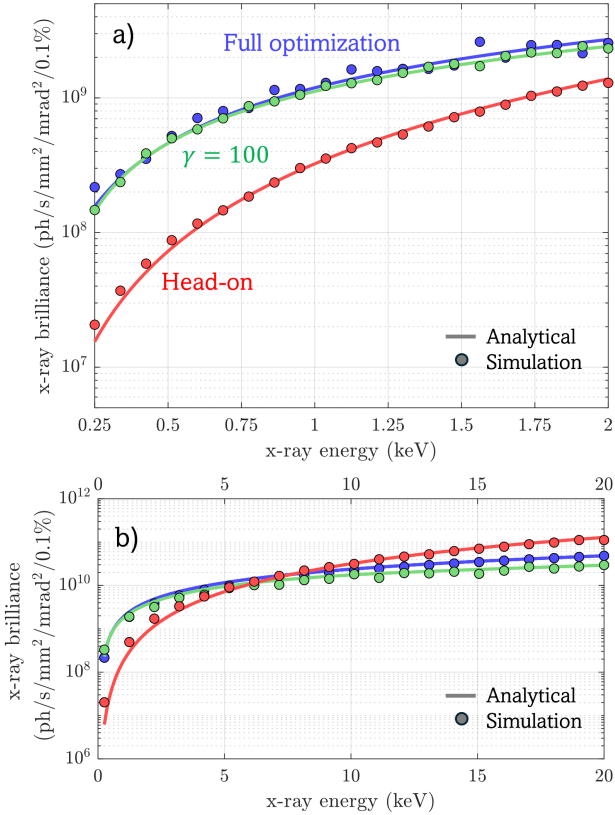


FIG. 10. X-ray brilliance for varying x-ray energies for three different geometries: head-on (red), grazing angle with full optimization (blue), and grazing angle with constant electron energy (green). a) shows the results for soft x-rays (0.25-2 keV) and b) shows the same result with the extension up to 20 keV.

We compare the x-ray source performance under three geometries. First, a full optimization as described in the previous section, where the electron energy, the interaction angle, and laser pulse shape are optimized. Second, an optimization of only the interaction angle, and laser pulse shape. Here the electron energy is constant. This has the advantage of no re-alignment of the electron optics, at the slight cost of performance. Finally, a head-on geometry optimized according to Sec. II. The corresponding x-ray brilliance throughout the x-ray energy range in the different geometries is shown in Fig. 10a. The dots show a comparison with particle tracking simulations (General Particle Tracer [32]) and subsequent numerical calculation of the Liénard-Wiechert potentials [33].

We find here that the grazing angle geometry is able to improve the brilliance of an ICS source by almost an order of magnitude in the soft x-ray regime. Additionally, the full optimization only differs slightly from the results of  $\gamma = 100$ . Fig. 10b shows the performance with the x-ray energy range continued to 20 keV. We find here

that the optimized head-on geometry outperforms the grazing angle geometry above 7 keV for the considered parameters.

The performance of the grazing angle geometry could be improved by utilizing an appropriate pulse front tilt, such that  $\zeta \rightarrow 1$ . The x-ray brilliance would in this case increase by approximately the aspect ratio of the laser pulse focus  $\sigma_{L\parallel}/\sigma_{L\perp} \simeq 2.15\sqrt{\omega_L\sigma_t/\psi_{\max}}$ .

Additionally the performance of the head-on geometry can be increased by using an appropriately chirped laser pulse to eliminate the effect of nonlinear broadening, which would reduce  $\chi \rightarrow 0$ .

#### IV. CONCLUSION

We have developed an analytical framework that optimizes the interaction geometry of an ICS x-ray source. In a head-on geometry a tight symmetrical laser pulse focus is required. The optimized laser spot size is primarily determined by the divergence of a focused laser pulse and the nonlinear broadening. In a grazing angle geometry we have found that an elliptical focus of the laser pulse is required to mitigate the reduced interaction time. Additionally the effects of laser pulse divergence and a three-dimensional electron bunch have been analyzed, resulting in a closed form expressions that allows the direct calculation of the laser pulse dimensions, interaction angle, and electron energy that optimize the x-ray brilliance. We find that this grazing angle geometry is especially useful for soft x-ray generation, a regime that is considered to be inefficient with conventional head-on scattering.

#### ACKNOWLEDGMENTS

We thank Brian Schaap for various fruitful discussions. This research was funded by Interreg Vlaanderen-Nederland (Smart\*Light project 2.0).

#### Appendix A: Derivation of the proper interaction time

We describe ICS in the framework of covariant electrodynamics, when electron recoil can be ignored ( $\hbar\omega_x/\gamma m_e c^2 \ll 1$ ), by assuming an electron with normalized 4-velocity  $u^\mu$  and 4-trajectory  $x^\mu$ , interacting with a laser pulse described by the normalized vector potential

$$A^\mu(\tau) = A_0 \exp(-\tau^2/2\tau_{\text{int}}^2) \exp[i\phi(\tau)]\epsilon^\mu, \quad (\text{A1})$$

with  $\phi(\tau) = k_L^\nu x_\nu(\tau)$  the laser phase and  $\epsilon^\mu$  is the laser 4-polarization. It is important to note that  $A^\mu$  describes the vector potential as experienced by the electron, i.e.

evaluated at the position and time described by the electron trajectory  $x^\mu$ . To arrive at Eq. (22) we assume that the amplitude vector potential remains small ( $A_0 \ll 1$ ) and that the laser pulse envelope varies slowly compared

to the laser phase. Additionally, we assume that the laser polarization is perpendicular to the initial electron 4-velocity  $u_0^\mu$ . The spectral angular density of the radiated field is given by [21]

$$\mathcal{S}(\omega, \theta_x) = \frac{\alpha A_0^2}{8\pi} \omega \tau_{\text{int}}^2 \exp \left[ -\gamma^2 \tau_{\text{int}}^2 (1 - \beta \cos \theta_x)^2 \left( \omega - \omega_L \frac{1 - \beta \cos \theta_L}{1 - \beta \cos \theta_x} \right)^2 \right] \left[ 1 - \left( \frac{\sin \theta_x \sin \varphi_x}{\gamma(1 - \beta \cos \theta_x)} \right)^2 \right], \quad (\text{A2})$$

with  $\varphi_x$  the polar angle of the emitted radiation. In the exponent we can directly identify the angular dependent Doppler shift of Eq. (1) and the Fourier limited bandwidth  $\Delta\omega/\omega_x = [\sqrt{2}\gamma(1 - \beta \cos \theta_L)\omega_L \tau_{\text{int}}]^{-1}$ . Evaluation of Eq. (A2) at  $\omega = \omega_x$  and  $\theta_x = 0$  results in Eq. (22). By integration over the x-ray frequency we find the angular radiation distribution

$$\frac{\partial N_x}{\partial \Omega} = \frac{\alpha A_0^2}{8\sqrt{\pi}} \frac{\omega_x \tau_{\text{int}}}{1 - \beta \cos \theta_x} \left[ 1 - \left( \frac{\sin \theta_x \sin \varphi_x}{\gamma(1 - \beta \cos \theta_x)} \right)^2 \right], \quad (\text{A3})$$

from which we can derive the characteristic  $1/\gamma$  cone. When  $u_0^\nu \epsilon_\nu \neq 0$ , this distribution changes. However, if  $\gamma \theta_L \gg 1$  this amounts to a rotation along  $\varphi_x$ .

To find the proper interaction time  $\tau_{\text{int}}$  we must describe the 3D laser pulse in Lorentz invariant quantities. For this we must introduce the following 4-vectors and corresponding invariant contractions:

$$\begin{aligned} \phi &= x_\nu k_L^\nu & k_L^\mu &= k(1, \hat{\mathbf{n}}) \\ \rho &= x_\nu r^\nu & r^\mu &= (0, \hat{\mathbf{e}} \times \hat{\mathbf{n}}) \\ \eta &= x_\nu \epsilon^\nu & \epsilon^\mu &= (0, \hat{\mathbf{e}}) \\ \varsigma &= x_\nu s^\nu & s^\mu &= (0, \hat{\mathbf{n}}) \end{aligned}$$

Figure 11 illustrates how the spatial components of these 4-vectors relate to the laser pulse. We note that, while  $r^\mu$  and  $s^\mu$  can be constructed in any reference frame, different observers may not construct the same 4-vectors. These vectors should therefore be interpreted as a tool to describe a laser pulse, rather than manifestly covariant 4-vectors.

We can now describe the vector potential as

$$A^\mu = A_0 \exp \left[ -\frac{\rho(\tau)^2}{4\sigma_{L\parallel}^2} - \frac{\eta(\tau)^2}{4\sigma_{L\perp}^2} - \frac{\phi(\tau)^2}{4\omega_L^2 \sigma_t^2} \right] \times \exp [i\phi(\tau)] \epsilon^\mu. \quad (\text{A4})$$

We now assume that the electron has a ballistic trajectory,  $x^\mu \simeq u_0^\mu c\tau$ , where defined that  $x_0^\mu = 0$ . This allows the vector potential to be rewritten as

$$A^\mu = A_0 \exp \left( -\left[ \frac{(u_0^\nu r_\nu)^2}{4\sigma_{L\parallel}^2} + \frac{(u_0^\nu k_{L\nu})^2}{4\omega_L^2 \sigma_t^2} \right] c^2 \tau^2 \right) \times \exp [i\phi(\tau)] \epsilon^\mu. \quad (\text{A5})$$

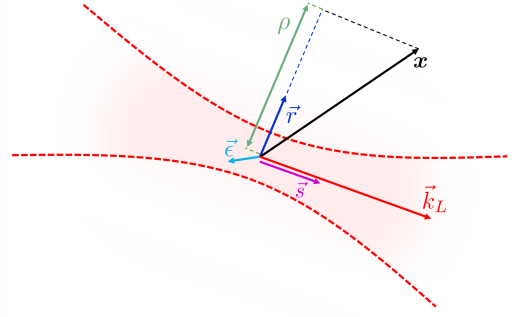


FIG. 11. Illustration of the spatial paths of  $k_L^\mu$ ,  $r^\mu$ ,  $\epsilon^\mu$  and  $s^\mu$ . The red curve represents the envelope of a Gaussian laser pulse.

Using  $u_0^\nu r_\nu = \gamma \beta \sin \theta_L$  and  $u_0^\nu k_{L\nu} = \gamma k_L (1 + \beta \cos \theta_L)$  the expression for the proper interaction time (Eq. (24)) can be identified. To incorporate the finite electron beam waist, we take  $x_0^\mu = (0, x_0, y_0, z_0)$  and integrate over the electron distribution.

Equation (A5) does not describe a true Gaussian TEM<sub>00</sub> mode. Importantly it lacks a description of the divergence, which can be corrected for using the substitution

$$A^\mu \rightarrow A^\mu / \sqrt{1 + (\varsigma/z_R)^2}. \quad (\text{A6})$$

Using  $\varsigma = u_0^\nu s_\nu c\tau = \gamma \beta \cos \theta_L c\tau$  we can identify the standard integral

$$\int d\tau \frac{\exp(-\tau^2/2\tau_{\text{int}}^2)}{\sqrt{1 + \tau^2/\tau_R^2}} = \tau_{\text{int}} \psi \exp(\psi^2/4) K_0(\psi^2/4), \quad (\text{A7})$$

with  $\psi = \tau_R/\tau_{\text{int}}$ . Comparing this to the Gaussian standard integral results in Eq. (26).

## Appendix B: Comparison with simulations

Throughout this paper, the developed theory has been checked with simulations. This is done by numerically calculating the spectral angular density from

the electron motion with Liénard-Wiechert potentials using the algorithm developed in [33]. The electron motion is calculated using a particle tracking simulation (General Particle Tracer [32]) and the electro-magnetic field descriptions of a pulsed Gaussian TEM<sub>00</sub> mode with a focus that can be asymmetrical.

This simulation not only takes into account a more accurate field description, that includes the radius of curvature, Gouy phase, and a diverging laser pulse, it also includes nonlinear effects and ponderomotive scattering. The electron beam is represented by 10<sup>3</sup> marcoparticles, where the effects of electron energy spread, divergence and beam size are incorporated. Since the dimen-

sions of the electron beam are much larger than the radiated wavelength, the contributions from individual marcoparticles have been added incoherently.

### Appendix C: Definition of x-ray brilliance

Throughout this paper we use the convention of r.m.s. x-ray brilliance, where  $\Delta A = \pi \langle x^2 + y^2 \rangle$ ,  $\Delta \Omega = \pi \langle \theta_x^2 \rangle$ , and  $\Delta \omega / \omega_x = \sqrt{\langle \omega^2 \rangle - \langle \omega \rangle^2} / \omega_x$  refer to r.m.s. quantities. Since we assume a Gaussian electron beam,  $\Delta A = 2\pi\sigma_e^2$ . However, since the radiation distribution to be approximately a uniform disk,  $\Delta \Omega = \pi\Theta_x^2/2$ . To convert the results from this paper to a FWHM convention, one can use  $B_x^{FWHM} = B_x / (2\sqrt{2 \ln 2})^3$ .

---

[1] P. Sedigh Rahimabadi, M. Khodaei, and K. R. Koswattage, Review on applications of synchrotron-based x-ray techniques in materials characterization, *X-Ray Spectrom.* **49**, 348 (2020).

[2] W. Thomlinson, H. Elleaume, L. Porra, and P. Suortti, K-edge subtraction synchrotron x-ray imaging in biomedical research, *Phys. Med.* **49**, 58 (2018).

[3] L. Quenot, S. Bohic, and E. Brun, X-ray phase contrast imaging from synchrotron to conventional sources: A review of the existing techniques for biological applications, *Appl. Sci.* **12**, 9539 (2022).

[4] M.-E. Couprie, New generation of light sources: Present and future, *J. Electron. Spectrosc. Relat. Phenom.* **196**, 3 (2014).

[5] B. Günther, R. Gradl, C. Jud, E. Eggli, J. Huang, S. Kulpe, K. Achterhold, B. Gleich, M. Dierolf, and F. Pfeiffer, The versatile x-ray beamline of the munich compact light source: design, instrumentation and applications, *J. Synchrotron Radiat.* **27**, 1395 (2020).

[6] Y. Du, L. Yan, J. Hua, Q. Du, Z. Zhang, R. Li, H. Qian, W. Huang, H. Chen, and C. Tang, Generation of first hard x-ray pulse at tsinghua thomson scattering x-ray source, *Rev. Sci. Instrum.* **84** (2013).

[7] K. Dupraz, M. Alkadi, M. Alves, L. Amoudry, D. Auguste, J.-L. Babigeon, M. Baltazar, A. Benoit, J. Bonis, J. Bonenfant, *et al.*, The thomx ics source, *Phys. Open* **5**, 100051 (2020).

[8] W. Graves, J. Bessuelle, P. Brown, S. Carbojo, V. Dolgashev, K.-H. Hong, E. Ihloff, B. Khaykovich, H. Lin, K. Murari, *et al.*, Compact x-ray source based on burst-mode inverse compton scattering at 100 khz, *Phys. Rev. ST Accel. Beams* **17**, 120701 (2014).

[9] I. J. M. V. Elk, C. W. Sweers, D. F. J. Nijhof, R. G. W. V. den Berg, T. G. Lucas, X. F. D. Stragier, P. Tack, M. N. Boone, O. J. Luiten, and P. H. A. Mutsaers, First x-rays from a compact and tunable linac-based compton scattering source, *Opt. Express* **33**, 47498 (2025).

[10] C. P. Barty, J. M. Algots, A. J. Amador, J. C. Barty, S. M. Betts, M. A. Castañeda, M. M. Chu, M. E. Dally, R. A. De Luna Lopez, D. A. Diviak, *et al.*, Design, construction, and test of compact, distributed-charge, x-band accelerator systems that enable image-guided, vhee flash radiotherapy, *Front. Phys.* **12**, 1472759 (2024).

[11] L. Amoudry, M. Kravchenko, R. Berry, N. Burger, A. Diego, J. Edelen, M. Ruelas, R. Agustsson, G. Andonian, Y.-C. Chen, *et al.*, Commissioning of a photocathode and interaction laser system at radiabeam compact inverse compton light source, *Nucl. Instrum. Methods Phys. Res. A: Accel. Spectrom. Detect. Assoc. Equip* **1075**, 170287 (2025).

[12] L. Faillace, R. G. Agostino, A. Bacci, R. Barberi, A. Bosotti, F. Broggi, P. Cardarelli, S. Cialdi, I. Drebot, V. Formoso, *et al.*, Status of compact inverse compton sources in italy: Brixs and star, in *Advances in Laboratory-based X-Ray Sources, Optics, and Applications VII*, Vol. 11110 (SPIE, 2019) pp. 14–21.

[13] T. Brümmer, S. Bohlen, F. Grüner, J. Osterhoff, and K. Pöder, Compact all-optical precision-tunable narrow-band hard compton x-ray source, *Sci. Rep.* **12**, 16017 (2022).

[14] V. Musat, P. Burrows, S. Doeberl, E. Granados, J. Herrador, A. Latina, and A. Malyzhenkov, A compact water window x-ray source based on inverse compton scattering (JACoW Publishing, 2024) pp. 441–444.

[15] B. Schaap, A. Murokh, and P. Musumeci, An inverse free electron laser-bunching driven shallow-angle superradiant compton source, *Nucl. Instrum. Methods Phys. Res. A: Accel. Spectrom. Detect. Assoc. Equip* **1066**, 169576 (2024).

[16] B. Günther, I. Kokhanovskyi, M. Dierolf, K. Achterhold, and F. Pfeiffer, Rapid x-ray energy switching for optimised k-edge subtraction imaging at narrow-band inverse compton x-ray sources, *Opt. Express* **33**, 47321 (2025).

[17] D. Berthe, L. Heck, S. Resch, M. Dierolf, J. Brantl, B. Günther, C. Petrich, K. Achterhold, F. Pfeiffer, S. Grandl, K. Hellerhoff, and J. Herzen, Grating-based phase-contrast computed tomography for breast tissue at an inverse compton source, *Sci. Rep.* **14**, 10.1038/s41598-024-77346-1 (2024).

[18] D. J. Batey, F. Van Assche, S. Vanheule, M. N. Boone, A. J. Parnell, O. O. Mykhaylyk, C. Rau, and S. Cipiccia, X-ray ptychography with a laboratory source, *Phys. Rev. Lett.* **126**, 193902 (2021).

[19] F. V. Hartemann and S. S. Wu, Nonlinear brightness optimization in compton scattering, *Phys. Rev. Lett.* **111**, 044801 (2013).

[20] E. Esarey, S. K. Ride, and P. Sprangle, Nonlinear thomson scattering of intense laser pulses from beams and plasmas, *Phys. Rev. E* **48**, 3003 (1993).

[21] B. H. Schaap, T. De Vos, P. Smorenburg, and O. J. Luiten, Photon yield of superradiant inverse compton scattering from microbunched electrons, *New J. Phys.* **24**, 033040 (2022).

[22] J. D. Jackson, *Classical electrodynamics*, 2nd ed. (Wiley, New York, NY, 1975).

[23] M. Furman, The moller luminosity factor (Lawrence Berkeley National Laboratory, 2003).

[24] D. Attwood, *Soft x-rays and extreme ultraviolet radiation: principles and applications* (Cambridge university press, 2000).

[25] V. Petrillo, A. Bacci, R. B. A. Zinati, I. Chaikovska, C. Curatolo, M. Ferrario, C. Maroli, C. Ronsivalle, A. Rossi, L. Serafini, *et al.*, Photon flux and spectrum of  $\gamma$ -rays compton sources, *Nucl. Instrum. Methods Phys. Res. A: Accel. Spectrom. Detect. Assoc. Equip.* **693**, 109 (2012).

[26] M. Abramowitz and I. A. Stegun, *Handbook of mathematical functions with formulas, graphs, and mathematical tables*, Vol. 55 (US Government printing office, 1948).

[27] F. V. Hartemann, F. Albert, C. W. Siders, and C. Barty, Low-intensity nonlinear spectral effects in compton scattering, *Phys. Rev. Lett.* **105**, 130801 (2010).

[28] B. Terzić, J. McKaig, E. Johnson, T. Dharanikota, and G. A. Krafft, Laser chirping in inverse compton sources at high electron beam energies and high laser intensities, *Phys. Rev. Accel. Beams* **24**, 094401 (2021).

[29] P. Pasmans, D. Van Vugt, J. Van Lieshout, G. Brussaard, and O. Luiten, Extreme regimes of femtosecond photoemission from a copper cathode in a dc electron gun, *Phys. Rev. Accel. Beams* **19**, 103403 (2016).

[30] T. G. Lucas, H.-H. Braun, P. Craievich, R. Fortunati, N. Kirchgeorg, A. Magazinik, M. Pedrozzi, J.-Y. Raguin, S. Reiche, M. Schaer, *et al.*, Toward a brightness upgrade to the swissfel: A high gradient traveling-wave rf photogun, *Phys. Rev. Accel. Beams* **26**, 103401 (2023).

[31] *PHAROS, Modular-Design Femtosecond Lasers for Industry and Science*, Light Conversion (2025).

[32] Pulsar Physics, General Particle Tracer (GPT), General Particle Tracer (GPT), <http://www.pulsar.nl/gpt>.

[33] A. Thomas, Algorithm for calculating spectral intensity due to charged particles in arbitrary motion, *Phys. Rev. ST Accel. Beams* **13**, 020702 (2010).

[34] K. Steiniger, M. Bussmann, R. Pausch, T. Cowan, A. Irman, A. Jochmann, R. Sauerbrey, U. Schramm, and A. Debus, Optical free-electron lasers with traveling-wave thomson-scattering, *J. Phys. B: At. Mol. Opt. Phys.* **47**, 234011 (2014).

[35] A. Potylitsyn, D. Gavrilenko, M. Strikhanov, and A. Tishchenko, Crab crossing in inverse compton scattering, *Phys. Rev. Accel. Beams* **26**, 040701 (2023).

[36] B. Schaap, M. Lenz, and P. Musumeci, Shallow angle inverse compton scattering, arXiv preprint arXiv:2509.04621 (2025).

[37] H. Zhang, Y. Du, Z. Chi, L. Yan, W. Huang, and C. Tang, Experimental demonstration of polarization control in thomson scattering x-ray sources, *Nucl. Instrum. Methods Phys. Res. A: Accel. Spectrom. Detect. Assoc. Equip.* **1064**, 169376 (2024).

[38] B. H. Schaap, C. W. Sweers, P. Smorenburg, and O. Luiten, Ponderomotive bunching of a relativistic electron beam for a superradiant thomson source, *Phys. Rev. Accel. Beams* **26**, 074401 (2023).

[39] M. Kördel, A. Dehlinger, C. Seim, U. Vogt, E. Fogelqvist, J. A. Sellberg, H. Stiel, and H. M. Hertz, Laboratory water-window x-ray microscopy, *Optica* **7**, 658 (2020).

[40] V. Weinhardt and C. Larabell, Soft x-ray tomography has evolved into a powerful tool for revealing cell structures, *Annu. Rev. Anal. Chem.* **18** (2025).

[41] C. Cao, M. F. Toney, T.-K. Sham, R. Harder, P. R. Shearing, X. Xiao, and J. Wang, Emerging x-ray imaging technologies for energy materials, *Mater. Today* **34**, 132 (2020).

[42] S. K. Beaumont, Soft xas as an in situ technique for the study of heterogeneous catalysts, *Phys. Chem. Chem. Phys.* **22**, 18747 (2020).

[43] T. Kimura, Y. Takeo, K. Sakurai, N. Furuya, S. Egawa, G. Yamaguchi, Y. Matsuzawa, T. Kume, H. Mimura, M. Shimura, *et al.*, Soft x-ray ptychography system using a wolter mirror for achromatic illumination optics, *Opt. Express* **30**, 26220 (2022).